frontiers | Frontiers in Soft Matter

TYPE Original Research
PUBLISHED 10 November 2023
DOI 10.3389/frsfm.2023.1281171

OPEN ACCESS

EDITED BY
Reza Foudazi,
University of Oklahoma, United States

REVIEWED BY
Muchu Zhou,
University of Oklahoma, United States
Hamed Salimi Kenari,
University of Mazandaran, Iran

*CORRESPONDENCE
Mark P. Andrews,
mark.andrews@mcgill.ca

RECEIVED 22 August 2023
ACCEPTED 25 October 2023
PUBLISHED 10 November 2023

CITATION
Chen X and Andrews MP (2023), Carboxylated cellulose nanocrystal cryogel monoliths: a multi-tool study of morphology and porosity of pure and magnetite nanoparticle-decorated CNC scaffolds.
Front. Soft Matter 3:1281171.
doi: 10.3389/frsfm.2023.1281171

Carboxylated cellulose nanocrystal cryogel monoliths: a multi-tool study of morphology and porosity of pure and magnetite nanoparticle-decorated CNC scaffolds

Xining Chen and Mark P. Andrews*

Department of Chemistry, McGill University, Montreal, QC, Canada

Tissue scaffolds are known to benefit from incorporation of nanoscale bio-additives like cellulose nanocrystals (CNC), which can affect porosity as an important tunable design parameter for bio-based scaffolds. In this paper, we probe how freeze-casting of carboxylated cellulose nanocrystals and CNC derivatized with magnetite nanoparticles yields macroscale cryogel scaffold monoliths. Cryogel topographical features and macropore morphologies depend on the conditions under which ice formation takes place, and on exposure to static magnetic fields. We examine porosity over several length scales with scanning electron microscopy (SEM) coupled with Local Thickness Euclidean distance image processing, small angle X-ray scattering (SAXS), and dynamic vapor sorption (DVS). SAXS data fitted with a mass fractal model and power law suggest that CNC particles aggregate to form well-defined compact walls in the range of 96.7–27.3 nm for all samples, while inclusion of Fe_3O_4 nanoparticles disrupts this compactness in the range of 27.3–4.8 nm. Analysis of DVS reveals that nanoparticles directly impact water uptake by the cryogel scaffolds and can reduce water sorption in mesopores with a radius of 5–6 nm.

KEYWORDS

tissue scaffold, cellulose nanocrystals, porosity, cryogel, nanoparticles, magnetic field effects, self-assembly

1 Introduction

Porous biopolymer scaffolds are widely investigated in the field of tissue repair and regeneration (Reddy et al., 2021). These types of scaffolds are known to benefit from nanoscale bio-inclusions like cellulose nanocrystals, generically known as CNC. The nanocrystals impart not only structural (mechanical) improvements but also enhanced bioactivity. Cellulose nanocrystals can be liberated from the nanocrystalline regions of cellulose microfibrils with proper combinations of mechanical forces, enzymes, strong acids or oxidizers (Lagerwall et al., 2014).

Whatever the method of production, the CNC isolate appears to be a desirable scaffold because it exhibits high crystallinity and significant hydrophilicity, robust mechanical strength, excellent biodegradability, low cytotoxicity and even bioactivity to a range of

animal and human cell types (Domingues et al., 2014)), and favorable interactions with cell lines (Imlimthan et al., 2020). These characteristics have made CNC attractive for bio-applications, acting for instance, as hosts for drug delivery (Akhlaghi et al., 2014; Ciolacu et al., 2016) and environments for cell cultures or tissue engineering (Or et al., 2019; Camarero-Espinosa et al., 2016; Osorio et al., 2019; Shaheen et al., 2019; Ferreira et al., 2020; Sun et al., 2021; Hong et al., 2021; N'Gatta et al., 2022). For example, in bone tissue engineering and growth, CNC has been shown to improve the mechanical properties and bioactivity of chitosan-alginate composites (Shaheen et al., 2019) and 3D printed CNC-polymer nanocomposites (Hong et al., 2021; N'Gatta et al., 2022). In addition, an aerogel bone tissue scaffolding, developed solely from chemically cross-linked cellulose nanocrystals, has been shown to promote bone-like cell proliferation and support the growth of hydroxyapatite on cell surfaces *in vitro* (Osorio et al., 2019). An extensive and detailed review by Szustak and Gendaszewska-Darmach discusses how nanocellulose scaffolds promote the development of cartilage tissue (Szustak and Gendaszewska-Darmach, 2021). More broadly, Ustunel et al. tackled the problem of matching scaffold stiffness to cell elasticity. In this case, CNC was used to tune polymer nanocomposite elastomer scaffold mechanical properties to adapt to the different viability requirements of neuroblastoma and fibroblast cells (Ustunel et al., 2021).

No universal scaffold construction exists that meets every need (Ferreira et al., 2020). Nevertheless, scaffold porosity emerges as an important and adaptable design parameter in scaffold production (Chen et al., 2020). Cells, genes, and proteins benefit from high porosity scaffolds to ensure their release and foster nutrient exchange environments. N'Gatta's research indicated that incorporating CNC can enhance polymer nanocomposite scaffold porosity by around 15% compared to the PLA host without additives (N'Gatta et al., 2022). In tissue engineering, controlling cell location and function after being introduced into the body is vital. Cell scaffolds provide a structural platform for cell attachment and proliferation and influence stem cell differentiation into targeted tissues (Bružauskaitė et al., 2016). Scaffold porosity, particularly pore size, shape, and interconnectivity, are integral for cell adhesion, interaction, transmigration, and growth (Bružauskaitė et al., 2016; Janmohammadi et al., 2023). Different pore sizes cater to various cellular interactions and migrations. For example, the regeneration of neurons requires long and narrow pore spaces that are hundreds of microns or even millimeters in length, but only 20–70 μm in width. Microvascular epithelial and smooth muscle cells can be accommodated in small 38 μm dimension pores (Bružauskaitė et al., 2016). To enhance cell function, pore interconnectivity is known to be vital for nutrient, oxygen, and waste exchange (Bružauskaitė et al., 2016; Janmohammadi et al., 2023). Pore shape in scaffolds also influences cell behavior and growth, implying that scaffolds should mimic the dimensional features of the guest cells (Phadke et al., 2013; Bružauskaitė et al., 2016; Camarero-Espinosa et al., 2016; Xu and Guan, 2016; Szustak and Gendaszewska-Darmach, 2021). Thus, although many cell types favor oval to round pore shapes (Bružauskaitė et al., 2016), cells with anisotropic, elongated cell shapes like those of musculoskeletal tissues and the outer meniscus, favor lamellar pores and channels (Phadke et al., 2013; Xu and Guan, 2016).

When it comes to drug delivery, especially with cellulosic materials, information about scaffold porosity and pore size is essential. Drug molecules are typically loaded onto scaffolds via physical entrapment and binding interactions through functional groups such as hydroxyl (Janmohammadi et al., 2023). Highly porous media offer greater surface area and binding sites, significantly affecting drug loading and release. For example, CNC combined with bone growth factors showed sustained release when loaded into biphasic calcium phosphate scaffold sponges. This benefit has been attributed to a reduction in porosity and pore size after incorporation of the nanocrystals and their slow degradation, both of which resulted in gradual drug diffusion (Sukul et al., 2015).

The topographic properties of scaffolds include not only porosity but also roughness and patterns. Aligned and randomly patterned scaffolds have different repair effects on various tissues (Chi et al., 2022). This gives incentive to use the anisotropic field response of CNC to impose topographic alignment in the scaffolds. Cellulose nanocrystals in solid films can be aligned by shear forces (Jinkins et al., 2021). CNC can also be forced to align into a chiral nematic liquid crystal phase; but this requires very high magnetic fields (ca. 17–28 T). Only recently, has it been shown that a weak magnetic field (≈0.5–1.2 T) will induce alignment of CNC through its diamagnetic response (Babaei-Ghazvini et al., 2020). Magnetite nanoparticles (Fe_3O_4) bound to CNC enhance nanocrystal magnetic susceptibility, making it easier to orient CNC at lower magnetic fields (Zhang et al., 2022). Incorporation of magnetite nanoparticles (MNP) into nanocellulose networks also helps expand its applications and better realize some existing functionalities (Islam et al., 2018). Independent of CNC, MNPs have been found to promote cell differentiation, proliferation, and growth when MNPs were present in scaffolds or loaded into cells (Aliramaji et al., 2017; Tomás et al., 2019; Torgbo and Sukyai, 2019; Labusca et al., 2020). Indeed, studies have demonstrated that application of an external magnetic field has positive effects on cells (Aliramaji et al., 2017; Tomás et al., 2019; Torgbo and Sukyai, 2019; Labusca et al., 2020); however, even without an applied magnetic field, the incorporation of superparamagnetic magnetic nanoparticles impacts cell behavior and the bioactivity of the scaffolds in beneficial ways (Aliramaji et al., 2017; Torgbo and Sukyai, 2019). In summary, it is reasonable to expect that the field response of CNC suspensions can be recruited to adjust the topographic properties of CNC.

Studies of porosity in the many different types of scaffolds have generally relied on scanning electron micrographs (Phadke et al., 2013; Shaheen et al., 2018; Or et al., 2019; Osorio et al., 2019), microcomputed tomography (Bertoldi et al., 2011), nitrogen sorption BET (Osorio et al., 2019), mercury intrusion porosimetry (Phadke et al., 2013), and liquid displacement using solvents (Shaheen et al., 2018). Combinations of these techniques have been deployed to contribute knowledge about the different types of scaffolds. Strengths and limitations of these individual techniques for interrogating scaffold porosity have been reviewed by Bertoldi (Bertoldi et al., 2011).

CNC can form self-supporting percolated physical networks via hydrogen-bonded interactions among individual particles assembled in colloidal form (Lewis et al., 2019). This state of rigid percolation differs from the entangled mesh networks created by many natural and

synthetic polymer chains as they bend and wrap around each other (Lewis et al., 2019). The propensity of CNC to percolate has been implemented to make physical hydrogels and aerogels via freeze-thawing or freeze-casting (Lewis et al., 2019; Munier et al., 2016). In freeze casting, solidification of the solvent induces a physical separation of nanocrystals from the suspending medium, and even shear alignment of CNC (Munier et al., 2016). Ice serves as a sacrificial template that is removed by freeze-drying. This step yields scaffolds of nanoparticle networks with an interconnected porous structure (Feirrera et al., 2020; Sun et al., 2021). Despite the importance of scaffold porosity in tissue engineering, the porosity and topographical features of CNC networks prepared by freeze casting of CNC or MNP-decorated CNC have seen no systematic study.

In passing, we note that the literature on CNC scaffolds has focused exclusively on sulfated CNC. In deference to the rising interest and commitment to matters of green chemistry, scalability and sustainability, the present study utilizes carboxylated CNC that is produced simultaneously during hydrolysis of Forest Stewardship Certified cellulose (Andrews and Morse, 2021; Lam and Hemraz, 2021). As noted by Harper et al. (2016) carboxylated cellulose nanocrystals have garnered attention for their versatility, with toxicity and biocompatibility profiles comparable to sulfated CNC. Reinforcing this observation, Pal et al. (2019) developed a nanocomposite film imbued with carboxylated CNC, exhibiting no cytotoxicity towards the HEK293 cell line, thereby highlighting its potential for biomedical applications. Unless otherwise stated, all cryogel experiments discussed in this paper refer to carboxylated CNC.

The research reported in this paper unites two facets of scaffolding with CNC. The first involves the combination of freeze-casting and magnetic field-directed templating to fabricate different topographies of large, porous CNC scaffold monoliths. The second brings a multi-tool characterization approach to the study of porosity and the topographic features of these CNC monoliths. We combine scanning, and transmission electron microscopy (SEM, TEM) with small angle x-ray scattering (SAXS), and dynamic vapor sorption (DVS) for surface area and equilibrium moisture (EMC) measurements. Image analysis using a Local Thickness Euclidean distance transformation was performed on SEM images of the cryogel scaffolds to obtain accurate estimates of minimum macropore sizes. Fractal dimensions, which quantify the complexity of a structure, were calculated from the SAXS data. For porous materials, the fractal dimension can provide insights into the scale-dependent nature of porosity, meaning how pore distribution varies from the nanoscale to the microscale (Anitas, 2018; Hossain et al., 2021). By combining analyses performed by SEM-local thickness transformations, SAXS, and DVS, our study aims to establish a reliable method to probe the morphology and the porosity of CNC-based cryogel scaffolds as renewable, biocompatible, and biodegradable porous scaffold materials.

The overall experimental scheme for fabricating and characterizing CNC-based cryogel scaffolds is shown in Figure 1.

2 Materials and methods

2.1 CNC and CNC-MNP suspensions

For these studies, a 100% Forest Stewardship Certified (FSC®) carboxylated CNC suspension of 3.8 wt% in water was provided by Anomera Inc. Nanocrystals were produced from black spruce (*Pica mariana*) by catalyst-free dilute hydrogen peroxide oxidation of dissolving pulp (Temalfa 93 N, Rayonier Advanced Materials, Temiscaming, Canada). The lightly carboxylated CNC (0.16 mmol/g) was used without further purification.

Carboxylated CNC, decorated with magnetite nanoparticles (CNC-MNP), was synthesized *in situ* by a co-precipitation method modified from the work of Hassan and coworkers (Hassan et al., 2019). Briefly, 20 mL of the CNC suspension was combined with 100 mL of MiliQ water (18.2 MOhm) and fully dispersed by sonication (6 mm Sonics Industries microtip in combination with a Sonics vibra-cell VCX 130 probe sonicator). A separate 10 mL aqueous solution of 1.0 mmol of $FeCl_2$ and two equivalents of $FeCl_3$ was prepared and slowly injected into the stirred CNC suspension under argon. The mixture was heated to 70°C for 1 hour before magnetite nanoparticles were co-precipitated by adding 1:10 diluted $NH_3OH_{(aq)}$. The product was washed many times using DI water until the wash reached a pH of 7. Excess water was removed by centrifuge at 500 rpm. (Higher rpm can lead to phase separation between the nanoparticles and CNC.) The compositions of the CNC and CNC-MNP particles were examined by X-ray Photoelectron Spectroscopy (XPS), and attachment of the MNP onto CNC was verified by Transmission Electron Microscopy (Section 1 in Supplementary Material).

2.2 CNC and CNC-MNP cryogels

CNC cryogels were prepared directly with the as-obtained 3.8 wt% CNC suspension in water. MNP-bound CNC cryogels were made from a mixture of 20% v/v of the as-synthesized MNP-decorated CNCs (CNC-MNP) and 80% v/v of as-obtained CNC suspension to give a gel phase similar to that of the CNC-only suspension. The mixed CNC/CNC-MNP suspension yielded a solid concentration of 3.9 %wt in water.

Gelation of the suspensions in glass vials was achieved by three different types of freezing. "High-temperature" freezing of the suspension was performed in a −12°C freezer, while "low-temperature" freezing was achieved by submerging the suspension in liquid nitrogen (LN2, -196°C). Two-step freezing was conducted first by freezing the sample at −12°C for 8 h, allowing the sample to thaw, then re-freezing the sample at liquid nitrogen temperature. This is a freeze-thaw-freeze experiment, followed by lyophilization. An external static magnetic field (SMF) was applied to some gelation processes using rectangular prism NdFeB permanent magnets (K&J magnetics). The surface field of each magnet was 0.1895 T centered on the axis of magnetization (See Supplementary Material). The magnets were aligned so that the magnetic field vectors were attractive between the planes of the magnets. The porous structure of the cryogel was obtained after freeze-drying for 48 h. Specifics of sample preparation are detailed in Section 2 of the Supporting Material.

2.3 Porosity study using SEM combined with "local thickness" quantitative image analysis tool, SAXS, and DVS

Macroscopic structural images of the cryogels were acquired by SEM. The SEM images were graphically fitted (Python) using the

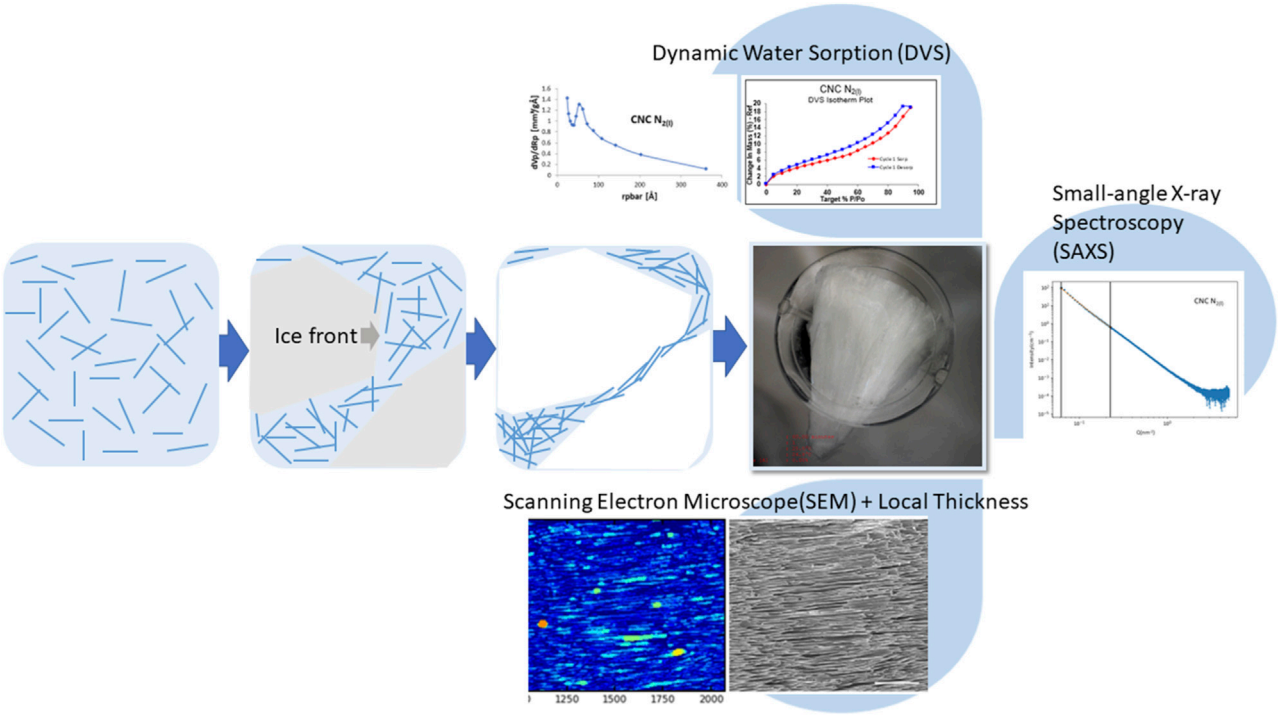

FIGURE 1
Flow scheme for fabricating and characterizing CNC-based cryogel scaffolds.

"Local Thickness" algorithm, PoreSpy. The algorithm provides lower-bound estimates of pore sizes (Chiang et al., 2009; Gostick et al., 2019; Yousseff et al., 2019). DVS and SAXS were performed to probe the microscopic structural details of the cryogels to assess their meso- and microporosities. Dynamic vapour sorption data were collected with a DVS Resolution instrument from Surface Measurement Systems. Small angle X-ray Scattering measurements were conducted with a SAXS point 2.0 instrument. The decay of the scattering intensity I(q) was fitted using a power law function and a surface fractal model, both available in the analysis program SasView. More details on the experimental methods on SEM-local thickness, SAXS, and DVS are available in Section 3, Section 4, and Section 5 of Supplementary Material.

3 Results and discussion

3.1 Impact of freezing protocol on scaffold topographical features: General findings

Figures 2 and 3 show SEM images of the various microporous scaffolds obtained under the 3 different freezing conditions. Discussion of magnetic nanoparticle and field effects is deferred to section 3.4. Supplementary Figure S3 details the Local Thickness calculation of macropore dimensions and their distributions. The cross-sections of all SEM images in Figures 2 and 3 give us qualitative insight into pore interconnectivity. Sectioning cleaves the encapsulated pore spaces exposing the thin edges of the CNC framework. One can therefore see the rather wide variation in strut thickness, strut spacing, anisotropy and density that depend on the method of scaffold production. The existence of interconnected interfaces in the scaffolds was confirmed by SAXS. The SAXS data are discussed in section 3.4. The most prominent morphological change is observed between the cryogel scaffold frozen at −12°C when compared with that frozen rapidly at liquid nitrogen temperature. The slow freezing process (high-temperature freezing) resulted in polydisperse rounded pore structures with large pore dimensions (Figures 2 and 3). Figure 4 shows a sample macropore size distribution derived by the Local Thickness method for the CNC cryogel scaffold frozen at −12°C. The morphology obtained by slowly cooling the CNC suspension to −12°C is consistent with the evolution of irreversibly agglomerated CNC particles nucleating and circumscribing unoriented ice crystals (Qian et al., 2009; Zhang H. et al., 2019). This interpretation makes sense since high temperature freezing is a slow freeze process, followed by freeze drying (lyophilization). Freezing at −12°C, concentrates the nanocrystals in water regions and promotes zones of 3-dimensional agglomeration among the CNC particles. The agglomerates are strongly stabilized via hydrogen bonding crosslinks. Water (as ice) is trapped within the cross-linked agglomerates. This gives rise to the large pores visible in the SEM micrograph. Similarly, two-step freezing is, in effect, a freeze (−12°C)-thaw-freeze (LN2 temperature)-freeze-drying (lyophilization) cycle. It has much in common with the pharmaceutical practice to enhance the chemical and physical stability of H-bonded networks to store and transport drugs (Bernal-Chávez et al., 2023). The morphology recorded in the

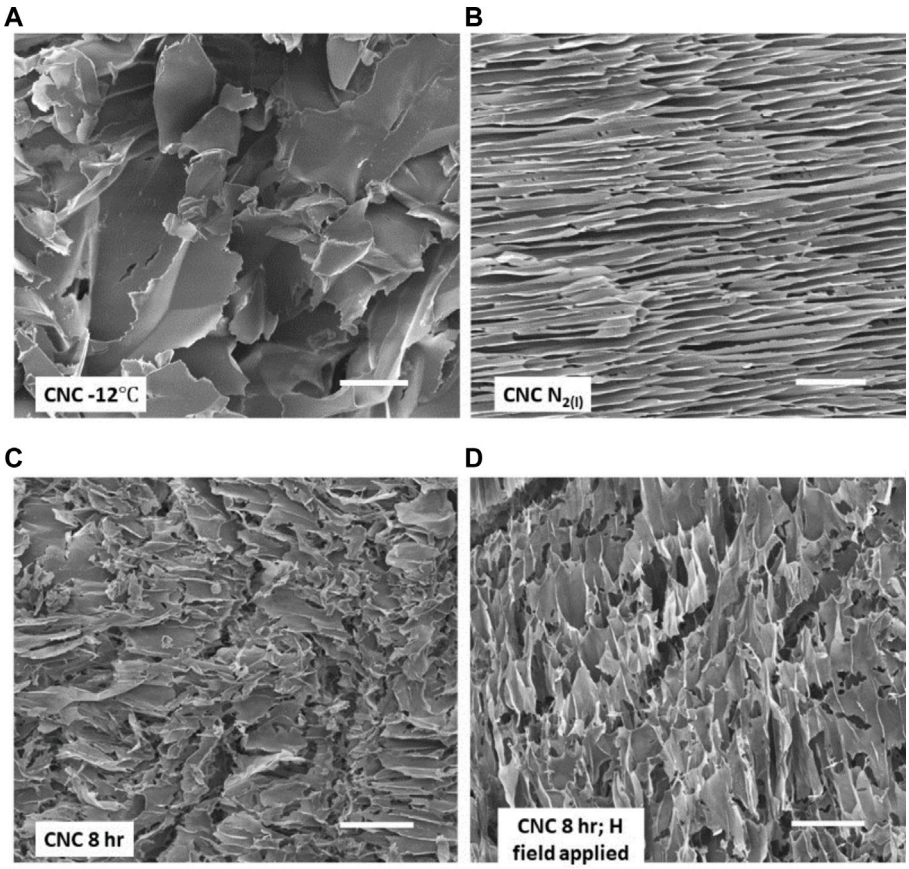

FIGURE 2
SEM images of four CNC cryogel scaffolds. **(A)** scaffold prepared by −12°C freezing of aqueous CNC suspension followed by freeze drying; **(B)** rapid freezing with LN2; **(C)** outcome of two-step freezing−freeze (−12°C)-thaw-freeze (LN2); **(D)** as in **(C)** but with magnetic field applied during both −12°C freeze and thaw steps. Scale bars on the images are each 50 μm. See text for details.

SEM image of Figure 2C differs from that in Figure 2A (single stage, −12°C freezing). The pores are smaller and there is evidence of orientational anisotropy in the pattern. As discussed below, the difference is due to the use of LN2 to freeze the sample in the second step of two-step freezing prior to lyophilization. The LN2 step introduces rapid radial growth of ice from the cylindrical vial wall to the centre. As discussed below, this process likely induces a shear field that partially aligns the nanocrystals.

Figure 2B (no MNP) and Figure 3B (with MNP) compare the scaffold topography after rapid freezing of CNC suspensions in liquid nitrogen. Both types of samples reveal compacted lamellar features with elongated pores. In both cases, the pore sizes peak in the range 10–13 μ m (Supplementary Figure S3). The tilt in the texture is real and not an artifact of sectioning the monolith.

The distinctive morphological differences between cryogel scaffolds produced by high- and low-temperature freezing can be explained only in part by the effects of temperature on heterogeneous ice nucleation. As discussed below, nucleation in our studies goes together with the response of the nanocrystals to magnetic fields (scalar magnetic pressure) and radially propagating crystal growth fronts. For completeness, we note that studies of ice nucleation and crystal growth have indicated that lower freezing temperatures lead to a higher degree of supercooling (Geidobler and Winter, 2013). With a higher degree of supercooling a greater number of ice crystals are nucleated and more water is instantly frozen (Rambhatla et al., 2004; Geidobler and Winter, 2013). In other words, fewer but larger ice crystals are expected when the freezing temperature is high, and numerous but smaller ice crystals are expected when the freezing temperature is low (Rambhatla et al., 2004; Geidobler and Winter, 2013).

Crystallization of water occurs with the production of porous structures when foreign particles are present in the freezing suspension. In our case, carboxylated CNC particles are rejected by the moving solidification fronts and are concentrated as cross-linked agglomerates that are trapped among the ice crystals (Lewis et al., 2019; Rambhatla et al., 2004; Qian et al., 2009; Zhang W. B. et al., 2019). The observation of lamellar morphology produced by low-temperature (LN2) freezing of aqueous cCNC, bears some similarity to the outcome of directional freezing of aqueous sulfated CNC (Munier et al., 2016). In that study, a Teflon mold containing a sulfated CNC suspension was cooled by contact with the tip of a copper cold-finger immersed in liquid nitrogen. This created a bottom-to-top temperature

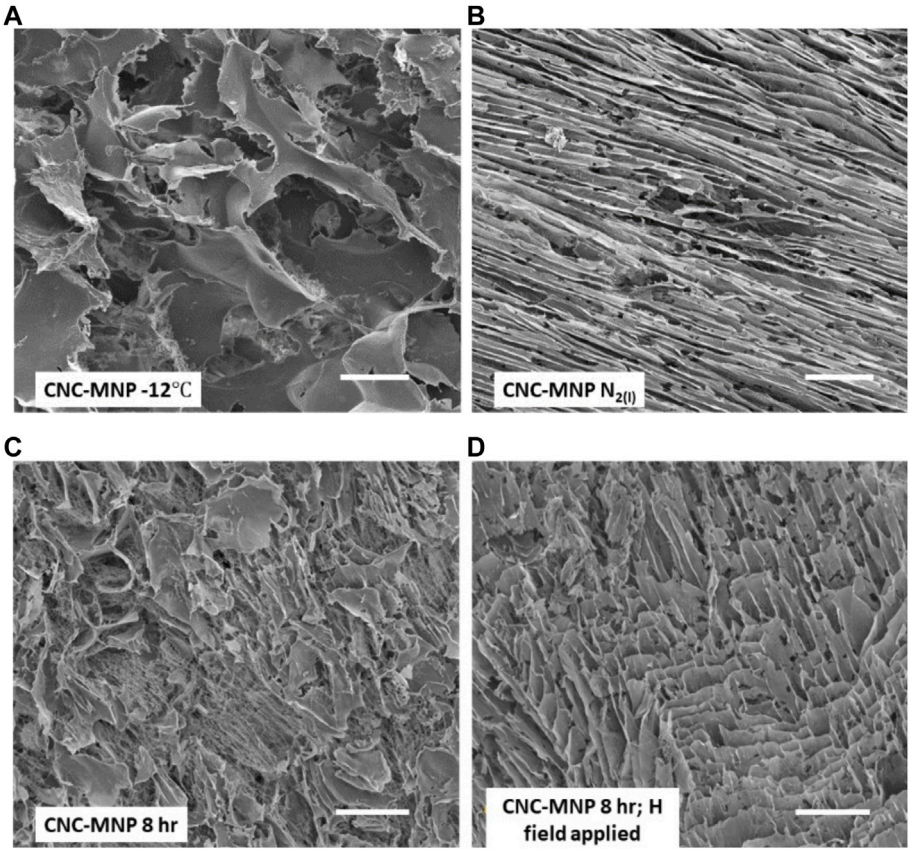

FIGURE 3
SEM images of four CNC-MNP cryogel scaffolds. **(A)** scaffold prepared by −12°C freezing of aqueous CNC-MNP suspension followed by freeze drying; **(B)** rapid freezing of CNC-MNP suspension with LN2; **(C)** outcome of two-step freezing−freeze (−12°C)-thaw-freeze (LN2); **(D)** as in **(C)** but with magnetic field applied during both −12°C freeze and thaw steps. Scale bars on the images are each 50 μm. See text for details.

gradient where the direction of freezing was longitudinal, producing alignment of the nanocrystals along a vertical axis. We did not intentionally design directional freezing into our experiment; nonetheless, we observed morphological outcomes that we attribute to directional freezing. Unlike the Munier experiment, we immersed the vial containing the CNC suspension directly into liquid nitrogen. This caused rapid freezing and flow of the ice front largely in the *radial* direction. With the smaller surface area of the base and the comparatively large volume of suspension above it, a slower rate of freezing is expected in the longitudinal direction. Indeed, by SEM (Figure 2B; Figure 3B), the CNC scaffold topography was aligned predominantly by radial freezing rather than by longitudinal freezing. This makes sense since radial cooling (freezing) of quiescent water in the cylindrical channel of the vial proceeds with rapid dendritic ice formation from the walls before transitioning to a solid ice annulus that grows radially inward (Jain et al., 2019). Our SEM images show that the nanocrystal strata (together with the pores) are tilted slightly away from the base of the vial. This tilt might be attributed to shear interaction between the vertical (longitudinal) and radial components of freezing. The different freezing configuration used by us *versus* Munier (Munier et al., 2016) suggests some additional versatility in applications of the directional freezing method to create alignment anisotropy in CNC scaffolds.

3.2 Scaffold topography after −12°C and 2-stage freezing with/without magnetic nanoparticles - no magnetic field

Figure 2A (no MNP) and Figure 3A (with MNP) compare representative SEM images of scaffold morphologies induced by −12°C freezing in the absence of a static magnetic field. Figure 2A (no MNP) reveals broad, leafy structures with some ragged and some smooth edges. Pore sizes are broad (Supplementary Figure S3, size distribution), maximizing in the range 35–75 μ m. Figure 3A was obtained for scaffolds produced from CNC decorated with magnetite nanoparticles. Qualitatively, the texture is more ragged and there is evidence of a fibrous network in the lower left quadrant of the image. The pore size is also broad, maximizing in the range 30–76 μ m. Fibrous structures were not detected in scaffolds produced by −12°C freezing in the absence of bound MNPs.

Figure 2C and Figure 3C contrast the results from 2-stage freezing. This procedure involved freezing a sample at −12°C for

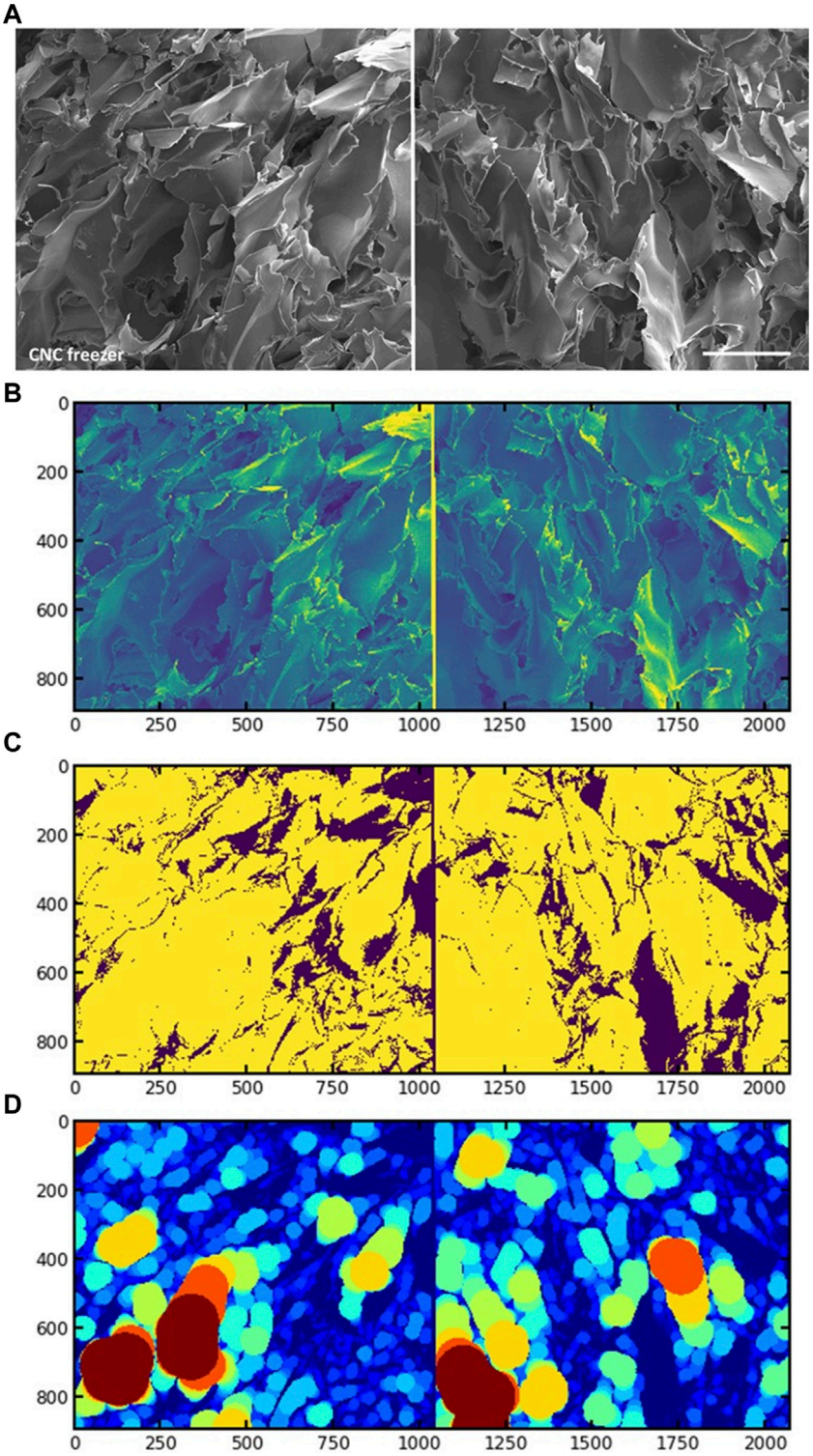

FIGURE 4
SEM image **(A)**, and Local Thickness algorithm read of the same SEM image **(B)**; inverted binary image by Otsu thresholding **(C)**; Local Thickness fitting **(D)**; and histogram of the pore diameter distribution against normalized volume fraction **(E)** of sample "CNC -12°C". All scale bars on **(A)** represent 100 *μm*. The yellow color evident in **(B)** indicates areas of emptiness, and the brown color indicates partitioning formed by the aggregation of CNC. Image analyses for all eight cryogel scaffolds are collected in Supplementary Figure S3.

8 h, allowing it to thaw (no agitation), then rapidly re-freezing the sample at liquid nitrogen temperature, followed by lyophilization. The scale bars in the images are identical. Clearly, when comparing the SEM images of Figures 2A, 2C or Figures 3A, 3C, the Figure 3C topographies are finer (less coarse) than those of the A images. Both images Figure 2C and Figure 3C hint at partial alignment of the

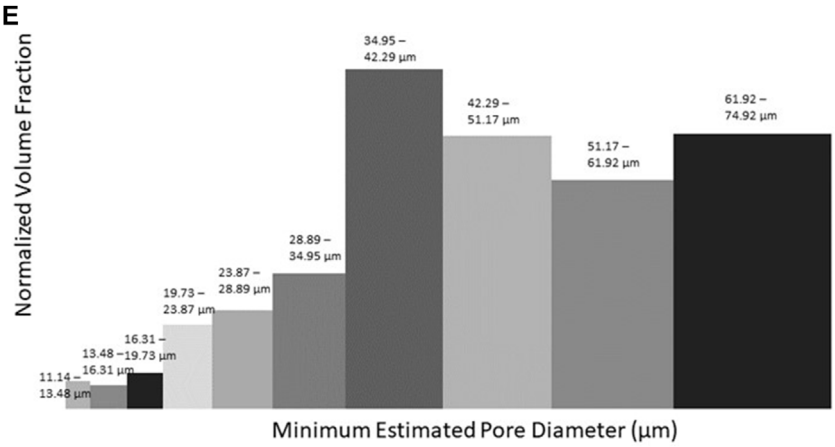

FIGURE 4
Continued.

texture. As described in section 3.1 above, evidence of alignment is unsurprising since the second stage of freezing uses liquid nitrogen, which causes radial freezing and directed alignment of CNC agglomerates in the previously thawed sample. With or without the magnetite nanoparticles, the pore sizes obtained with 2-stage freezing are smaller and more narrowly distributed. Supplementary Figure S3 (8 h, 2-stage) gives peak pore sizes in the range 10–18 μ m (no MNP), and in the range 13–15 μ m (with MNP). There is evidence of a fibrous network in Figure 3C (with MNP) that is not evident when texture is formed from CNC without attached magnetite nanoparticles.

3.3 Scaffold topography after −12°C and 2-stage freezing - With magnetic field

The effects of applying a static magnetic field (SMF, H-field) to the CNC and CNC-MNP suspensions were examined for the case of high temperature (−12°C) and 2-stage freezing. The magnets were positioned parallel, face-to-face, to create an attractive field with the magnetic field vectors pointing towards one another (Supplementary Scheme S1). We did not examine other magnet configurations. For the single step high temperature experiment, the CNC suspension was exposed to the H-field as it cooled to −12°C. Water was then removed from the solid sample by freeze-drying. For two-step freezing, the SMF was applied during the −12°C first stage of the two-stage freezing protocol. The sample was then thawed in the field of the magnets, after which they were removed. The sample was then plunged into liquid nitrogen.

We first compare the effects of the SMF on samples with and without MNPs. SEM images of sections from the monoliths are found in Figure 2D (two-step, no MNP) and 3D (two-step, with MNP). In Figure 2D, there is clear evidence of alignment *after* exposure to the SMF according to the 2-stage protocol. This SMF-directed response of CNC in water is consistent with the findings of Babaei-Ghazvini (Babaei-Ghazvini et al., 2020). They showed that CNC could be aligned with a weak magnetic field in the mobile phase of starch nanocomposites. Note that structural alignment in the CNC scaffold is approximately in the direction of the magnetic field vectors. We theorize that the CNC particles respond through their anisotropic diamagnetic susceptibility to the H-field. Nanocrystal alignment in this manner would enhance hydrogen bonding cross-links among CNCs; hence, to agglomerates that conspire with the radially propagating ice crystal front. It is these agglomerates that are oriented in the radial freezing field induced by LN2. In this case, the pore size peaks in the range 14–16 μ m (Supplementary Figure S3). Additional SEM images can be viewed by consulting Supplementary Figure S3 for images labeled CNC 8 h H-field applied.

There is clearly a difference in the layer texture of the CNC scaffolds that are generated from exposure to the SMF. The reader is encouraged to compare the SEM images in Supplementary Figure S3 for the 2-stage protocol (CNC 8 h H field applied and CNC-MNP 8 h H field applied). The addition of MNPs to the CNC leads to dense lamellar (sheet) packing in the presence of the SMF. This differs from the texture observed when CNC *without* MNPs is exposed to the H-field in the 2-stage freezing study. Evidently, binding MNPs to the CNC surfaces enhances their superparamagnetic response to the SMF (Zhang et al., 2022). Superparamagnetic nanoparticles align their spin vector in the direction of the field. MNPs bound to the CNC surfaces will respond to the SMF by aligning the nanocrystals to which they are bound. This effect is documented on the bulk scale for one of our CNC-MNP samples in Supplementary Figure S2.

Finally, it is also instructive to compare the layered texture of Figure 2D with that exhibited by CNC subjected to the 2-stage protocol, but without the applied field (Figure 2C). The difference between the 2 images is that alignment in the absence of the H-field (Figure 2C) is driven solely by the propagating radial freezing front under the LN2 impulse. Despite the apparent differences in the texture and alignment, the pore sizes with and without the H field are similar. By our previous arguments, this finding does not mean that the weak magnetic field has no effect on the scaffold topography. If topography comprises porosity, roughness and patterning (Chi et al., 2022) then despite the similarities in porosity, roughness and patterning emerge as differentiators

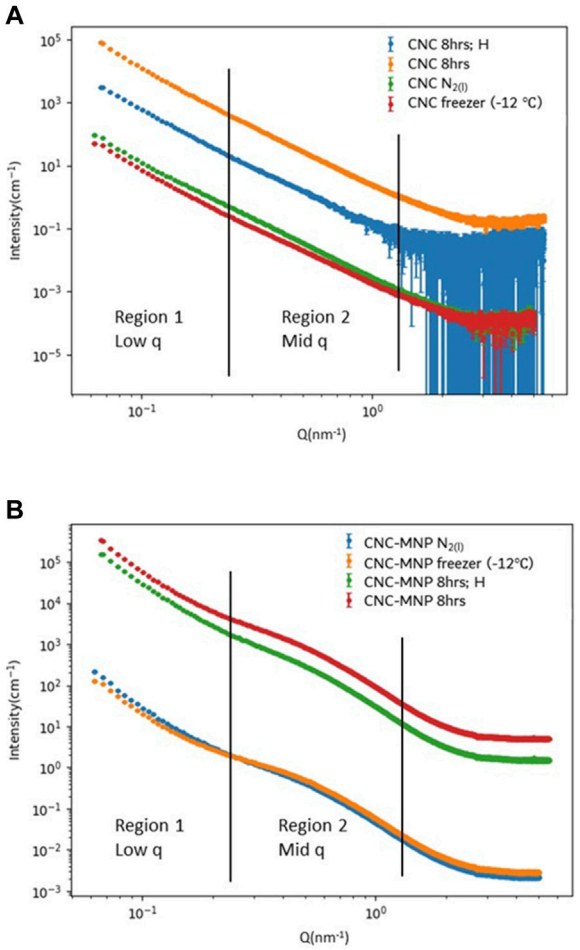

FIGURE 5
Small-angle X-ray (SAXS) measurements of **(A)** CNC and **(B)** CNC-MNP cryogel scaffolds.

when scaffolds are created in the absence *versus* the presence of a weak magnetic field.

3.4 Investigating nanoscale structures using SAXS

SAXS curves for CNC and CNC-MNP cryogel scaffolds are shown in Figures 4A, B, respectively. The *x*-axis of the SAXS curves is the scattering vector q, which relates to the inverse length scale, $2\pi/q$ (Zhang H. et al., 2019). As such, the noise-excluding q range between q_{min} = 0.065 and q_{max} = 1.3 nm^{-1} in this experiment gives nanoscale information in the range of 96.7–4.83 nm. Two q ranges of interest were examined, namely, the low-q region (Figure 5, region 1) between 96.7–27.3 nm, and the mid-q region (Figure 5, region 2) between 27.3–4.83 nm. In the low-q region, the slope of the scattering curve of all CNC and CNC-MNP cryogel scaffolds displayed $I(q) \propto q^{-4}$ power-law decay. The q^{-4} power law suggests that the CNC objects aggregate to form distinctive interfaces and well-defined shapes (Houssain et al., 2020), which is indeed observed by our SEM images of aggregated CNC sheets. The sheets make up the walls of the macroporous scaffolds (Figure 4, Supplementary Figure S3). Moving towards the mid-q region, the power law relations deviated from q^{-4}. The mass fractal dimensions calculated for the mid-q region are 2.9 for all pure CNC samples. For samples with incorporated MNPs, the mass fractal dimensions reduced to 2.1–2.3 (Supplementary Table S2), indicating a decrease in the compactness of the network structure (Anitas, 2018; Hossain et al., 2021). This aligns with the presence of small pores in the size range of 27.3–4.83 nm. The compactness is lower for CNC-MNP samples, likely due to the accommodation of nanoparticles.

3.5 Water vapor sorption study using DVS

The cryogel scaffolds expand with increasing water uptake and contract as moisture is removed (Supplementary Figure S5). The adsorption isotherm for each cryogel scaffold is shown in Supplementary Figure S6. The water vapor adsorption/desorption isotherms for different CNC cryogels are all type IV(a) isotherms with H2(b) hysteresis loops according to IUPAC classification (Thommes et al., 2015). Type IV(a) isotherms with H2(b) hysteresis loops correspond to mesoporous adsorbents with monolayer-multilayer adsorption and possible pore condensation.

Mesopore differential plots were calculated for all scaffolds based on precise water vapor pressure and gravimetric measurements. The results are shown in Supplementary Figure S7. Building on the SAXS observations, where the scattering intensity suggested the presence of specific nanoscale structures, the DVS measurements further elucidate the scale of porosity in the scaffolds. The mesopores determined from the DVS data have radii ranging from 2–36 nm. This size range encompasses but exceeds the mid-q region observed in SAXS. However, the majority of water sorption takes place in small pores since the volume occupied increases with decreasing pore size. Most of the pore volume in DVS can be attributed to mesopores with radii of 15 nm or less (Supplementary Figure S7). This conclusion is consistent with the mid-q region observed in SAXS.

It was found that the freezing methods or an applied SMF had little effect on water sorption mesoporosity, while the incorporation of MNPs induced a change to the mesoporosity pattern. While the water sorption volume generally increased with decreasing pore size within the probed range of mesoporosity, a sorption peak occurred at a mesopore radius of 5–6 nm for scaffolds made only with CNC, which the CNC-MNP scaffolds do not share. The MNPs synthesized *in situ* were polydispersed nanoparticles approximately 4–12 nm in diameter (Supplementary Figure S1D). The lack of a sorption peak in CNC-MNP scaffolds may indicate space occupied by MNPs.

The percent change in sample mass by adsorption and desorption of water vapor over time reveals the equilibrium moisture content (EMC) and the sorption kinetics pattern of the cryogel scaffolds. Despite the difference in compositions (CNC vs. CNC-MNP) and macroporosity, the cryogel scaffolds show similar adsorption kinetics (Figure 6A). The EMC for different cryogel samples falls within the water uptake range of 17.6%–20.0%. CNC cryogel scaffolds show slightly higher EMC than CNC-MNP cryogel scaffolds, as shown in Figure 6B. BET surface areas, calculated based on water as an absorbent, showed that CNC scaffolds have slightly higher surface areas compared to their CNC-MNP counterparts (Supplementary Table S3).

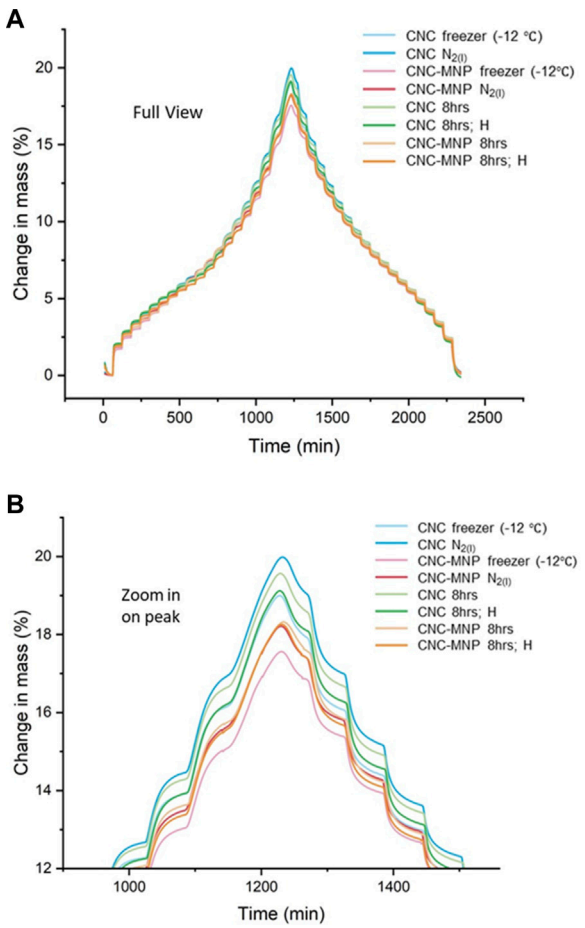

FIGURE 6
(A) Percent change in sample mass relative to reference mass *versus* running time in an adsorption and desorption cycle at 95% relative humidity (approximately between 0%–97% in actual % partial pressure). **(B)** is a zoom-in view of the turning point from adsorption to desorption, where EMC of the cryogel scaffolds occurs.

The narrow hysteresis curves of water sorption for all cryogel scaffolds (Supplementary Figure S6) examined in this experiment are comparable to those identified elsewhere for CNC with low amorphous content and high crystallinity (Guo et al., 2017). With crystalline solids, water adsorbs on the surface as monolayers and up to three to six layers (Sheokand et al., 2014). In a study of Stöber silica spheres, it was estimated that about 4 layers of water can adsorb on the surfaces at 25°C and $p/p_0 = 0.89$ (Farrando-Pérez et al., 2018; Gallego-Gómez et al., 2020). Water also penetrates pore structures and causes swelling, likely due to interactions with hydroxyl groups at the CNC-water interface (Mihranyan et al., 2004; Guo et al., 2017; Farrando-Pérez et al., 2018). The swelling, in turn, opens new sites for water sorption (Guo et al., 2017; Farrando-Pérez et al., 2018; Gallego-Gómez et al., 2020).

4 Conclusion

The combination of SEM with Local Thickness Euclidean distance image processing, SAXS, and DVS provided insight into both macro- and mesoporosity in CNC-based cryogel scaffolds. High (−12°C) freezing temperatures resulted in large, unoriented pores, while low (77 K) freezing temperatures resulted in narrow, lamellar, and oriented pores. Two-step freezing combining high-temperature cryogelation and low-temperature freezing produced slightly widened pore diameters, but reduced pore orientation compared with those made with low-temperature freezing alone. SAXS confirmed that the scaffolds have interconnected interfaces in the range of 96.7–27.3 nm, while the involvement of MNPs disrupted the compact aggregation in 27.3–4.8 nm. Water sorption mesoporosity in the cryogel scaffolds (radius of 2–36 nm) was unaffected by the choice of freezing method. DVS revealed that CNC-MNP scaffolds have less volume occupied by mesopores of radius 5–6 nm, and have slightly lower EMC than their CNC-only counterpart. At high freezing temperatures, an applied static magnetic field was shown to impose some degree of ordering in scaffold topography through CNC anisotropic diamagnetic response, or the superparamagnetic response of CNC with surface-bound magnetite nanoparticles. We showed that knowledge of changes to scaffold topography can benefit from a multi-tool analysis approach involving SEM imaging and image processing, in combination with dynamic vapor sorption and small angle X-ray scattering.

Data availability statement

The original contributions presented in the study are included in the article/Supplementary Materials, further inquiries can be directed to the corresponding author.

Author contributions

MA: Funding acquisition, Investigation, Project administration, Resources, Supervision, Validation, Writing–review and editing. XC: Conceptualization, Investigation, Methodology, Writing–original draft.

Funding

The author(s) declare financial support was received for the research, authorship, and/or publication of this article. This work was supported by the Natural Sciences and Engineering Research Council of Canada (NSERC) under grant RGPIN-2018-05912. This work benefited from the use of the SasView application, originally developed under NSF award DMR-0520547. SasView contains code developed with funding from the European Union's Horizon 2020 research and innovation programme under the SINE2020 project, grant agreement No. 654000.

Acknowledgments

We thank Hatem Titi, Research Associate and X-Ray facility manager at the McGill Chemistry Characterization Facility (MC2), for DVS and SAXS data collection as well as proofreading this manuscript. The authors gratefully acknowledge additional support from the Centre québécois sur les matériaux fonctionnels/Quebec

Centre for Advanced Materials (CQMF/QCAM) and the McGill Facility for Electron Microscopy Research (FEMR).

Conflict of interest

MA is a co-founder and shareholder of Anomera Inc, which donated the cCNC used in this research. He is a co-inventor on the patented process required to make cCNC.

The remaining author declares that the research was conducted in the absence of any commercial or financial relationships that could be construed as a potential conflict of interest.

The author(s) declared that they were an editorial board member of Frontiers, at the time of submission. This had no impact on the peer review process and the final decision.

Publisher's note

Supplementary material

The Supplementary Material for this article can be found online at: https://www.frontiersin.org/articles/10.3389/frsfm.2023.1281171/full#supplementary-material

References

Akhlaghi, S. P., Tiong, D., Berry, R. M., and Tam, K. C. (2014). Comparative release studies of two cationic model drugs from different cellulose nanocrystal derivatives. *Eur. J. Pharm. Biopharm.* 88 (1), 207–215. doi:10.1016/j.ejpb.2014.04.012

Aliramaji, S., Zamanian, A., and Mozafari, M. (2017). Super-paramagnetic responsive silk fibroin/chitosan/magnetite scaffolds with tunable pore structures for bone tissue engineering applications. *Mater. Sci. Eng. C* 70, 736–744. doi:10.1016/j.msec.2016.09.039

Andrews, M., and Morse, T. (2021). *Method for producing functionalized nanocrystalline cellulose and functionalized nanocrystalline cellulose thereby produced*. U.S. Patent No US 10,968,283. Washington, DC, USA: U.S. Patent and Trademark Office.

Anitas, E. M. (2018). "Small-angle scattering from mass and surface fractals," in *Complexity in biological and physical systems-bifurcations, Solitons and fractals* (London, UK: Intechopen), 169–189.

Babaei-Ghazvinia, A., Cudmoreb, B., Dunlopa, M., Acharyaa, B., Bissessurb, R., Ahmeda, M., et al. (2020). Effect of magnetic field alignment of cellulose nanocrystals in starch nanocomposites: physicochemical and mechanical properties. *Carbohydr. Polym.* 247, 116688. doi:10.1016/j.carbpol.2020.116688

Bernal-Chávez, S. A., Romero-Montero, A., Hernández-Parra, H., Peña-Corona, S. I., Del Prado-Audelo, M. L., Alcalá-Alcalá, S., et al. (2023). Enhancing chemical and physical stability of pharmaceuticals using freeze-thaw method: challenges and opportunities for process optimization through quality by design approach. *J. Biol. Eng.* 17, 35. doi:10.1186/s13036-023-00353-9

Bertoldi, S., Farè, S., and Tanzi, M. (2011). Assessment of scaffold porosity: the new route of micro-ct. *J. Appl. Biomaterials Biomechanics* 9 (3), 165–175. doi:10.5301/jabb.2011.8863

Bružauskaitė, I., Bironaitė, D., Bagdonas, E., and Bernotienė, E. (2016). Scaffolds and cells for tissue regeneration: different scaffold pore sizes—different cell effects. *Cytotechnology* 68 (3), 355–369. doi:10.1007/s10616-015-9895-4

Camarero-Espinosa, S., Rothen-Rutishauser, B., Weder, C., and Foster, E. J. (2016). Directed cell growth in multi-zonal scaffolds for cartilage tissue engineering. *Biomaterials* 74, 42–52. doi:10.1016/j.biomaterials.2015.09.033

Chen, H., Han, Q., Wang, C., Liu, Y., Chen, B., and Wang, J. (2020). Porous scaffold design for additive manufacturing in orthopedics: a review. *Front. Bioeng. Biotechnol. Sect. Biomechanics* 8, 609. doi:10.3389/fbioe.2020.00609

Chi, J., Wang, M., Chen, J., Hu, L., Chen, Z., Backman, L. J., et al. (2022). Topographic orientation of scaffolds for tissue regeneration: recent advances in biomaterial design and applications. *Biomimetics* 7, 131. doi:10.3390/biomimetics7030131

Chiang, M. Y., Landis, F. A., Wang, X., Smith, J. R., Cicerone, M. T., Dunkers, J., et al. (2009). Local thickness and anisotropy approaches to characterize pore size distribution of three-dimensional porous networks. *Tissue Eng. Part C. Methods* 15 (1), 65–76. doi:10.1089/ten.tec.2008.0298

Ciolacu, D., Rudaz, C., Vasilescu, M., and Budtova, T. (2016). Physically and chemically crosslinked cellulose cryogels: structure, properties and application for controlled release. *Carbohydr. Polym.* 151, 392–400. doi:10.1016/j.carbpol.2016.05.084

Domingues, R. M., Gomes, M. E., and Reis, R. L. (2014). The potential of cellulose nanocrystals in tissue engineering strategies. *Biomacromolecules* 15 (7), 2327–2346. doi:10.1021/bm500524s

Farrando-Pérez, J., López, C., Silvestre-Albero, J., and Gallego-Gómez, F. (2018). Direct measurement of microporosity and molecular accessibility in stober spheres by adsorption isotherms. *J. Phys. Chem. C* 122 (38), 22008–22017. doi:10.1021/acs.jpcc.8b07278

Ferreira, F. V., Otoni, C. G., Kevin, J., Barud, H. S., Lona, L. M., Cranston, E. D., et al. (2020). Porous nanocellulose gels and foams: breakthrough status in the development of scaffolds for tissue engineering. *Mater. Today* 37, 126–141. doi:10.1016/j.mattod.2020.03.003

Gallego-Gómez, F., Farrando-Pérez, J., López, C., and Silvestre-Albero, J. (2020). Micropore filling and multilayer formation in stober spheres upon water adsorption. *J. Phys. Chem. C* 124 (38), 20922–20930. doi:10.1021/acs.jpcc.0c05313

Geidobler, R., and Winter, G. (2013). Controlled ice nucleation in the field of freeze-drying: fundamentals and technology review. *Eur. J. Pharm. Biopharm.* 85 (2), 214–222. doi:10.1016/j.ejpb.2013.04.014

Gostick, J. T., Khan, Z. A., Tranter, T. G., Kok, M. D., Agnaou, M., Sadeghi, M., et al. (2019). PoreSpy: a python toolkit for quantitative analysis of porous media images. *J. Open Source Softw.* 4 (37), 1296. doi:10.21105/joss.01296

Guo, X., Wu, Y., and Xie, X. (2017). Water vapor sorption properties of cellulose nanocrystals and nanofibers using dynamic vapor sorption apparatus. *Sci. Rep.* 7 (1), 14207–14212. doi:10.1038/s41598-017-14664-7

Harper, B. J., Clendaniel, A., Sinche, F., Way, D., Hughes, M., Schardt, J., et al. (2016). Impacts of chemical modification on the toxicity of diverse nanocellulose materials to developing zebrafish. *Cellulose* 23, 1763–1775. doi:10.1007/s10570-016-0947-5

Hassan, A., Sorour, N. M., El-Baz, A., and Shetaia, Y. (2019). Simple synthesis of bacterial cellulose/magnetite nanoparticles composite for the removal of antimony from aqueous solution. *Int. J. Environ. Sci. Technol.* 16, 1433–1448. doi:10.1007/s13762-018-1737-4

Hong, J., Cooke, S., Whittington, A., and Roman, M. (2021). Bioactive cellulose nanocrystal-poly(ε-caprolactone) nanocomposites for bone tissue engineering applications. *Front. Bioeng. Biotechnol.* 9, 605924. doi:10.3389/fbioe.2021.605924

Hossain, L., Raghuwanshi, V. S., Tanner, J., and Garnier, G. (2021). Modulating nanocellulose hydrogels and cryogels strength by crosslinking and blending. *Colloids Surfaces A Physicochem. Eng. Aspects* 630, 127608. doi:10.1016/j.colsurfa.2021.127608

Imlimthan, S., Correia, A., Figueiredo, P., Lintinen, K., Balasubramanian, V., Airaksinen, A. J., et al. (2020). Systematic *in vitro* biocompatibility studies of multimodal cellulose nanocrystal and lignin nanoparticles. *J. Biomed. Mater. Res. Part A* 108 (3), 770–783. doi:10.1002/jbm.a.36856

Islam, M. S., Chen, L., Sisler, J., and Tam, K. C. (2018). Cellulose nanocrystal (CNC)–inorganic hybrid systems: synthesis, properties and applications. *J. Mater. Chem. B* 6 (6), 864–883. doi:10.1039/c7tb03016a

Jain, A., Miglani, A., Huang, Y., Weibel, J., and Garimella, S. (2019). Ice formation modes during flow freezing in a small cylindrical channel. *Int. J. Heat Mass Transf.* 128, 836–848. doi:10.1016/j.ijheatmasstransfer.2018.08.051

Janmohammadi, M., Nazemi, Z., Salehi, A. O. M., Seyfoori, A., John, J. V., Nourbakhsh, M. S., et al. (2023). Cellulose-based composite scaffolds for bone tissue engineering and localized drug delivery. *Bioact. Mater.* 20, 137–163. doi:10.1016/j.bioactmat.2022.05.018

Jin, S., Sun, S., Jiang, X., Zhao, Y., Wang, Y., and Deng, Y. (2020). Effect of static magnetic field on the freezing process of deionized water and 0.9% NaCl solution. *J. Food Process. Preserv.* 44 (9), e14663. doi:10.1111/jfpp.14663

Jinkins, K., Wang, J., Dwyer, J., Wang, X., and Arnold, M. (2021). Confined shear alignment of ultrathin films of cellulose nanocrystals. *ACS Appl. Bio Mater.* 4 (11), 7961–7966. doi:10.1021/acsabm.1c00884

Labusca, L., Herea, D. D., Danceanu, C. M., Minuti, A. E., Stavila, C., Grigoras, M., et al. (2020). The effect of magnetic field exposure on differentiation of magnetite

nanoparticle-loaded adipose-derived stem cells. *Mater. Sci. Eng. C* 109, 110652. doi:10.1016/j.msec.2020.110652

Lagerwall, J. P., Schütz, C., Salajkova, M., Noh, J., Park, J. H., Scalia, G., et al. (2014). Cellulose nanocrystal-based materials: from liquid crystal self-assembly and glass formation to multifunctional thin films. *NPG Asia Mater.* 6 (1), e80. doi:10.1038/am.2013.69

Lam, E., and Hemraz, U. D. (2021). Preparation and surface functionalization of carboxylated cellulose nanocrystals. *Nanomaterials* 11 (7), 1641. doi:10.3390/nano11071641

Leung, A. C. W., Hrapovic, S., Lam, E., Liu, Y., Male, K. B., Mahmoud, K. A., et al. (2011). Characteristics and properties of carboxylated cellulose nanocrystals prepared from a novel one-step procedure. *Small* 7, 302–305. doi:10.1002/smll.201001715

Mihranyan, A., Llagostera, A. P., Karmhag, R., Strømme, M., and Ek, R. (2004). Moisture sorption by cellulose powders of varying crystallinity. *Int. J. Pharm.* 269 (2), 433–442. doi:10.1016/j.ijpharm.2003.09.030

Munier, P., Gordeyeva, K., Bergstrom, L., and Fall, A. B. (2016). Directional freezing of nanocellulose dispersions aligns the rod-like particles and produces low-density and robust particle networks. *Biomacromolecules* 17 (5), 1875–1881. doi:10.1021/acs.biomac.6b00304

N'Gatta, K., Belaid, H., El Hayek, J., Assanvo, E., Kajdan, M., Masquelez, N., et al. (2022). 3D printing of cellulose nanocrystals based composites to build robust biomimetic scaffolds for bone tissue engineering. *Sci. Rep.* 12, 21244. doi:10.1038/s41598-022-25652-x

Or, T., Saem, S., Esteve, A., Osorio, D. A., De France, K. J., Vapaavuori, J., et al. (2019). Patterned cellulose nanocrystal aerogel films with tunable dimensions and morphologies as ultra-porous scaffolds for cell culture. *ACS Appl. Nano Mater.* 2 (7), 4169–4179. doi:10.1021/acsanm.9b00640

Osorio, D. A., Lee, B. E., Kwiecien, J. M., Wang, X., Shahid, I., Hurley, A. L., et al. (2019). Crosslinked cellulose nanocrystal aerogels as viable bone tissue scaffolds. *Acta Biomater.* 87, 152–165. doi:10.1016/j.actbio.2019.01.049

Pal, N., Banerjee, S., Roy, P., and Pal, K. (2019). Reduced graphene oxide and PEG-grafted TEMPO-oxidized cellulose nanocrystal reinforced poly-lactic acid nanocomposite film for biomedical application. *Mater. Sci. Eng. C* 104, 109956. doi:10.1016/j.msec.2019.109956

Phadke, A., Hwang, Y., Kim, S. H., Kim, S. H., Yamaguchi, T., Masuda, K., et al. (2013). Effect of scaffold microarchitecture on osteogenic differentiation of human mesenchymal stem cells. *Eur. cells Mater.* 25, 114–129. doi:10.22203/ecm.v025a08

Qian, L., Ahmed, A., Foster, A., Rannard, S. P., Cooper, A. I., and Zhang, H. (2009). Systematic tuning of pore morphologies and pore volumes in macroporous materials by freezing. *J. Mater. Chem.* 19 (29), 5212–5219. doi:10.1039/b903461g

Rambhatla, S., Ramot, R., Bhugra, C., and Pikal, M. J. (2004). Heat and mass transfer scale-up issues during freeze drying: II. Control and characterization of the degree of supercooling. *AAPS Pharmscitech* 5 (4), 54–62. doi:10.1208/pt050458

Reddy, M., Ponnamma, D., Choudhary, R., and Sadasivuni, K. (2021). A comparative review of natural and synthetic biopolymer composite scaffolds. *Polymers* 13, 1105. doi:10.3390/polym13071105

Shaheen, T., Montaser, A., and Li, S. (2019). Effect of cellulose nanocrystals on scaffolds comprising chitosan, alginate and hydroxyapatite for bone tissue engineering. *Int. J. Biol. Macromol.* 121, 814–821. doi:10.1016/j.ijbiomac.2018.10.081

Sheokand, S., Modi, S. R., and Bansal, A. K. (2014). Dynamic vapor sorption as a tool for characterization and quantification of amorphous content in predominantly crystalline materials. *J. Pharm. Sci.* 103 (11), 3364–3376. doi:10.1002/jps.24160

Sukul, M., Nguyen, T., Min, Y.-K., Lee, S.-Y., and Lee, B.-T. (2015). Effect of local sustainable release of BMP2-VEGF from nano-cellulose loaded in sponge biphasic calcium phosphate on bone regeneration. *Tissue Eng. Part A* 21 (11-12), 1822–1836. doi:10.1089/ten.tea.2014.0497

Sun, Y., Chu, Y., Wu, W., and Xiao, H. (2021). Nanocellulose-based lightweight porous materials: a review. *Carbohydr. Polym.* 255, 117489. doi:10.1016/j.carbpol.2020.117489

Szustak, M., and Gendaszewska-Darmach, E. (2021). Nanocellulose-based scaffolds for chondrogenic differentiation and expansion. *Front. Bioeng. Biotechnol.* 9, 736213. doi:10.3389/fbioe.2021.736213

Thommes, M., Kaneko, K., Neimark, A. V., Olivier, J. P., Rodriguez-Reinoso, F., Rouquerol, J., et al. (2015). Physisorption of gases, with special reference to the evaluation of surface area and pore size distribution (IUPAC Technical Report). *Pure Appl. Chem.* 87 (9-10), 1051–1069. doi:10.1515/pac-2014-1117

Tomás, A. R., Gonçalves, A. I., Paz, E., Freitas, P., Domingues, R. M., and Gomes, M. E. (2019). Magneto-mechanical actuation of magnetic responsive fibrous scaffolds boosts tenogenesis of human adipose stem cells. *Nanoscale* 11 (39), 18255–18271. doi:10.1039/c9nr04355a

Torgbo, S., and Sukyai, P. (2019). Fabrication of microporous bacterial cellulose embedded with magnetite and hydroxyapatite nanocomposite scaffold for bone tissue engineering. *Mater. Chem. Phys.* 237, 121868. doi:10.1016/j.matchemphys.2019.121868

Torkashvand, N., and Sarlak, N. (2019). Fabrication of a dual T1 and T2 contrast agent for magnetic resonance imaging using cellulose nanocrystals/Fe3O4 nanocomposite. *Eur. Polym. J.* 118, 128–136. doi:10.1016/j.eurpolymj.2019.05.048

Ustunel, S., Prevot, M., Rohaley, G., Webb, C., Yavitt, B., Freychet, G., et al. (2021). Mechanically tunable elastomer and cellulose nanocrystal composites as scaffolds for *in vitro* cell studies. *Mat. Adv.* 2, 464–476. doi:10.1039/d0ma00676a

Vanderfleet, O., D'Acierno, F., Isogai, A., MacLachlan, M., Michal, M., and Cranston, D. (2022). Effects of surface chemistry and counterion selection on the thermal behavior of carboxylated cellulose nanocrystals. *Chem. Mat.* 34, 8248–8261. doi:10.1021/acs.chemmater.2c01665

Xu, Y., and Guan, J. (2016). "Interaction of cells with polyurethane scaffolds," in *Advances in polyurethane biomaterials* (Sawston, United Kingdom: Woodhead Publishing), 523–542.

Youssef, A., Hrynevich, A., Fladeland, L., Balles, A., Groll, J., Dalton, P. D., et al. (2019). The impact of melt electrowritten scaffold design on porosity determined by x-ray microtomography. *Tissue Eng. Part C. Methods* 25 (6), 367–379. doi:10.1089/ten.tec.2018.0373

Yu, H., Abdalkarim, S., Zhang, H., Wang, C., and Tam, K. (2019). Simple process to produce high-yield cellulose nanocrystals using recyclable citric/hydrochloric acids. *ACS Sustain. Chem. Eng.* 7 (5), 4912–4923. doi:10.1021/acssuschemeng.8b05526

Zhang, H., Liu, C., Chen, L., and Dai, B. (2019a). Control of ice crystal growth and its effect on porous structure of chitosan cryogels. *Chem. Eng. Sci.* 201, 50–57. doi:10.1016/j.ces.2019.02.026

Zhang, W. B., Wang, X. D., Kong, Q. G., Ruan, H. J., Zuo, X. B., Ren, Y., et al. (2019b). Power–law feature of structure in metallic glasses. *J. Phys. Chem. C* 123 (45), 27868–27874. doi:10.1021/acs.jpcc.9b07168

Zhang, X., Kang, S., Adstedt, K., Kim, M., Xiong, R., Yu, J., et al. (2022). Uniformly aligned flexible magnetic films from bacterial nanocelluloses for fast actuating optical materials. *Nat. Commun.* 13, 5804. doi:10.1038/s41467-022-33615-z

Zhou, Y., Saito, T., Bergström, L., and Isogai, A. (2018). Acid-free preparation of cellulose nanocrystals by TEMPO oxidationand subsequent cavitation. *Biomacromolecules* 19, 633–639. doi:10.1021/acs.biomac.7b01730